Emergence of electron coherence and two-color all-optical switching in MoS_2 based on spatial self-phase modulation

Yanling Wu, Qiong Wu, Fei Sun, Cai Cheng, Sheng Meng[1], and Jimin Zhao[1]

Beijing National Laboratory for Condensed Matter Physics and Institute of Physics, Chinese Academy of Sciences, Beijing 100190, China

Edited by Roberto Merlin, University of Michigan, Ann Arbor, Michigan, and accepted by the Editorial Board July 25, 2015 (received for review March 11, 2015)

Generating electron coherence in quantum materials is essential in optimal control of many-body interactions and correlations. In a multidomain system this signifies nonlocal coherence and emergence of collective phenomena, particularly in layered 2D quantum materials possessing novel electronic structures and high carrier mobilities. Here we report nonlocal ac electron coherence induced in dispersed MoS_2 flake domains, using coherent spatial self-phase modulation (SSPM). The gap-dependent nonlinear dielectric susceptibility $\chi^{(3)}$ measured is surprisingly large, where direct interband transition and two-photon SSPM are responsible for excitations above and below the bandgap, respectively. A wind-chime model is proposed to account for the emergence of the ac electron coherence. Furthermore, all-optical switching is achieved based on SSPM, especially with two-color intraband coherence, demonstrating that electron coherence generation is a ubiquitous property of layered quantum materials.

electron coherence | transition metal dichalcogenide | self-phase modulation | optical switching | emergent phenomena

Recently 2D layered quantum materials have attracted tremendous interest since the discovery of graphene a decade ago (1). Various layered materials, ranging from boron nitride sheets to transition metal dichalcogenides and from topological insulators to high-temperature superconductors, have been intensively investigated (2–11). Strict 2D atomic crystals can now be produced at a macroscopic scale, using a variety of methods (11, 12). Among them molybdenum disulfide (MoS_2) and related layered quantum materials are particularly interesting due to their novel optical properties and potential valleytronics applications (4, 5, 8, 9) at a thickness of monolayer and few layers (2, 10, 13). Layered materials share common physical properties rooted in their ubiquitous 2D quantum nature, for which achieving pure coherence among electrons (lattices) is of particular interest (14–19). The presence of multiple domains is ubiquitous in many known 2D quantum materials, ranging from stripe-order cuprate superconductors to polycrystalline strongly correlated systems. For example, phase locking between different layers of stripe orders is crucial for enhancing the superconducting phase in layered high-temperature superconductors (20, 21).

In this work we demonstrate unambiguously that nonlocal and intraband ac electron coherence, of which the electronic wave function oscillates at an optical frequency of 10^{14} Hz, can be generated in separate MoS_2 flakes, using spatial self-phase modulation (SSPM). The SSPM is a coherent third-order nonlinear optical process systematically investigated decades ago (22), where the nonlinear optical susceptibility $\chi^{(3)}$ is uniquely determined by the laser-intensity-dependent refractive index $n = n_0 + n_2 I$, where n_0 and n_2 are linear and nonlinear refractive indexes, respectively. If this effect is strong enough in a material, the phenomenon of self-focusing can be directly observed. The SSPM is also frequently referred to as the optical Kerr effect or the ac Kerr effect (note the difference from the regular Kerr effect). It is parallel to the other third-order nonlinear optical processes, such as third harmonic generation (THG) and four-wave mixing (FWM).

Our investigations show that gap-dependent SSPM is a general method for inducing electron coherence in 2D layered materials. Monolayer and few-layer MoS_2 (and other similar layered materials) have finite bandgaps, which lift the obstacle to versatile electronic and optical applications (2, 23, 24). Because SSPM using below-gap photons has not been reported, MoS_2 provides an ideal test platform for observing SSPM in finite-bandgap materials. A model has been developed to account for the coherence emergence process and theoretical calculations have been carried out to unravel the underlying mechanism. Moreover, we demonstrate all-optical switching based on SSPM, which employs intraband electron coherence. This optical switch has multiple advantages, including weak-control-strong performance, cascade-possible, and high-contrast two-color switching.

Results and Discussion

Fig. 1 displays the experimental setup and typical SSPM patterns obtained from the flake domains of MoS_2 in a suspension (*Methods*). It can be seen from Fig. 1*B* that the sample is mainly composed of MoS_2 flakes with a thickness of 30 ~ 55 layers. In Fig. 1 *D–F* we show the SSPM patterns obtained using 400-nm ultrafast laser pulses, 532-nm continuous wave (cw) laser beams, and 800-nm ultrafast laser pulses, respectively. The SSPM is a nonlinear optical process in that the phase (rather than the intensity) of the output beam depends on the input intensity (*Methods*).

Significance

Generating electron coherence is nontrivial in that most sophisticated electronic experimental methods are noncoherent or cannot be used to induce and detect collective states. By using coherent spatial self-phase modulation (SSPM) (a nonlinear optical property) we observed the emergence of electron coherence in a gapped quantum material, MoS_2. By observing gap-dependent SSPM we discovered that it is a ubiquitous property of two-dimensional layered quantum materials. Furthermore, we demonstrate that this ac electron coherence can be harnessed to realize two-color all-optical switching with superb performance.

Author contributions: J.Z. designed research; Y.W., Q.W., F.S., and J.Z. performed research; C.C. and S.M. obtained theoretical absorption; Q.W. and J.Z. derived wind chime model; Y.W., S.M., and J.Z. analyzed data; and S.M. and J.Z. wrote the paper.

The authors declare no conflict of interest.

This article is a PNAS Direct Submission. R.M. is a guest editor invited by the Editorial Board.

Freely available online through the PNAS open access option.

[1]To whom correspondence may be addressed. Email: jmzhao@iphy.ac.cn or smeng@iphy.ac.cn.

This article contains supporting information online at www.pnas.org/lookup/suppl/doi:10.1073/pnas.1504920112/-/DCSupplemental.

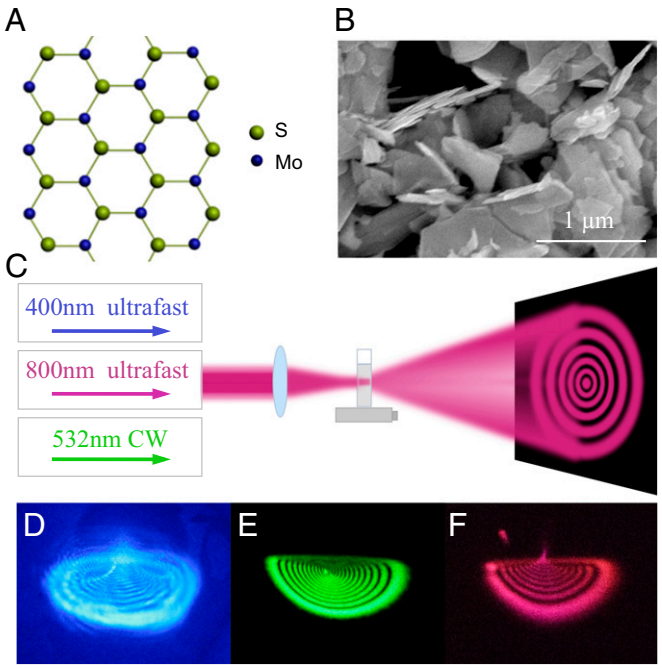

Fig. 1. (*A*) Schematic lattice structure of MoS_2. (*B*) Scanning electron microscopy image of the MoS_2 flakes. (*C*) Schematic experimental setup. (*D–F*) The SSPM patterns generated using 400-nm, 532-nm, and 800-nm laser beams, respectively.

To unambiguously verify that we have observed SSPM, we performed intensity-dependence measurements. Fig. 2 shows that the number of rings N increases nearly linearly with the laser intensity, until the saturation is reached. By this linear dependence the optical nonlinear coefficient n_2, hence $\chi^{(3)}$, can be obtained directly (Fig. 2 and *Methods*). Because nearly all of the light is diffracted off the incidence direction and the Rayleigh scattering is low, ideally it is a purely coherent third-order nonlinear optical process. This pure coherence must originate from the coherence within the sample—the electron coherence, where the electronic wave function preserves a definite phase (see discussion below). In the case that photoexcited carriers become out of phase due to collisions, impurity scatterings, and boundary reflections, they reassume their coherence transiently (at a timescale of femtoseconds) under the external light pulse.

Next we consider nonlocal electron coherence. In our sample, each flake is a domain. Charge carriers in any form (including photocarriers, excitons, free electron–hole pairs, and intrinsic electrons and holes) in different and the same domains are initially completely out of phase. Besides, each domain has an arbitrary orientation. Upon light interaction, photoinduced quasiparticles interact with the electric field (Fig. 3*A*) and assume its local phases.

We propose a wind-chime model to describe the emergence of electron coherence from the nonlocal domains driven by SSPM (Fig. 3*A*). Initially there exists an arbitrary orientation angle θ between a MoS_2 flake (thus the electrical polarization it contains) and the electric field. Due to energy relaxation, the electric field reorients the flakes so that each domain contains an axis parallel to the polarization of the external field, as if each domain is "hung" by a vertical "thread." This image mimics that of a wind chime (Fig. 3*A*). Once the wind chime is formed, the electron coherence is completely set up within and among each of the different domains. This scenario depicts the emergence of nonlocal electron coherence as a complex collective behavior.

We first show that the model is reasonable. Assuming a circular disk shape for the MoS_2 flake domains, we derived (*SI Text, section S1*) that the rotation torque generated by the laser pulse $\mathcal{M} = \int |\boldsymbol{P}\times\boldsymbol{E}|\,dV$ has a magnitude of

$$\mathcal{M} = \frac{1}{4}\sin 2\theta\,\frac{(\varepsilon_r - 1)}{\varepsilon_r}\,\varepsilon_0 E_0^2 \pi R^2 h e^{-\left(2(ct-z)^2/c^2\tau^2\right)}, \qquad [1]$$

where R is the disk radius, h is the disk thickness, and τ is the pulse width. Taking the Newton fluid with constant viscosity coefficient η and linear velocity v at the interface, the rotation torque $\mathcal{V}$ due to the viscous force is

$$\mathcal{V} = \eta \int_0^{\pi} \frac{dv}{dr}(R\sin\varphi)(\xi\cdot 2\pi R\sin\varphi)(Rd\varphi) = \pi\eta\Omega\xi R^3, \qquad [2]$$

where Ω is the rotation velocity and ξ is the portion of the fluid globe that is rotating together with the disk. Hence the rotation angle accumulated due to each single light pulse is (*SI Text, section S1*)

$$\delta\theta = \int_0^T \Omega\,dt \approx \int_0^{\infty} \Omega_0 e^{-\left(\pi\eta\xi R^3/\left(J_{MoS_2}+J_{Solution}\right)\right)t} dt = \frac{(\varepsilon_r - 1)}{\varepsilon_r}\,\frac{2TIh}{4\eta\xi Rc}\sin 2\theta, \qquad [3]$$

where T is the repetition period. The time needed for the pattern formation is (*SI Text, section S1*)

$$\mathcal{T} = \frac{\varepsilon_r \pi\eta\xi Rc}{1.72(\varepsilon_r - 1)Ih} = 0.3\ s, \qquad [4]$$

where we have used the values $\varepsilon_r = 3.33$ for MoS_2, $\eta = 3.2\times10^{-4}$ Pa•s for acetone, $R \sim 1$ μm, $h \sim 10$ nm, $I = 250$ W/cm^2, and $\xi \sim 0.03$ in our experiment. As a result, $\mathcal{T}$ does not depend on T. Thus, for both pulsed and cw excitations the results are identical, which has been verified in our experiment. To compare with the experiment, we recorded the formation processes of the ring patterns (see snapshots in Fig. 3 *B* and *C*). The ring number and diameter both increase monotonously with time until the maximum is reached after 0.20 s. This compares well with the predicted value by the wind-chime model. Thus, the observed

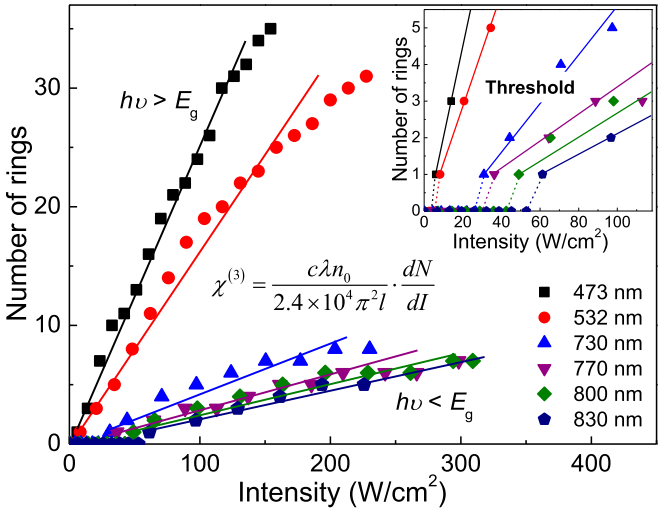

Fig. 2. Intensity dependence of ring numbers and bandgap dependence of $\chi^{(3)}$. The slopes directly illustrate the nonlinear coefficients $\chi^{(3)}$. The solid lines are guides to the eye. (*Inset*) The thresholds to observe the SSPM patterns at different photon energies.

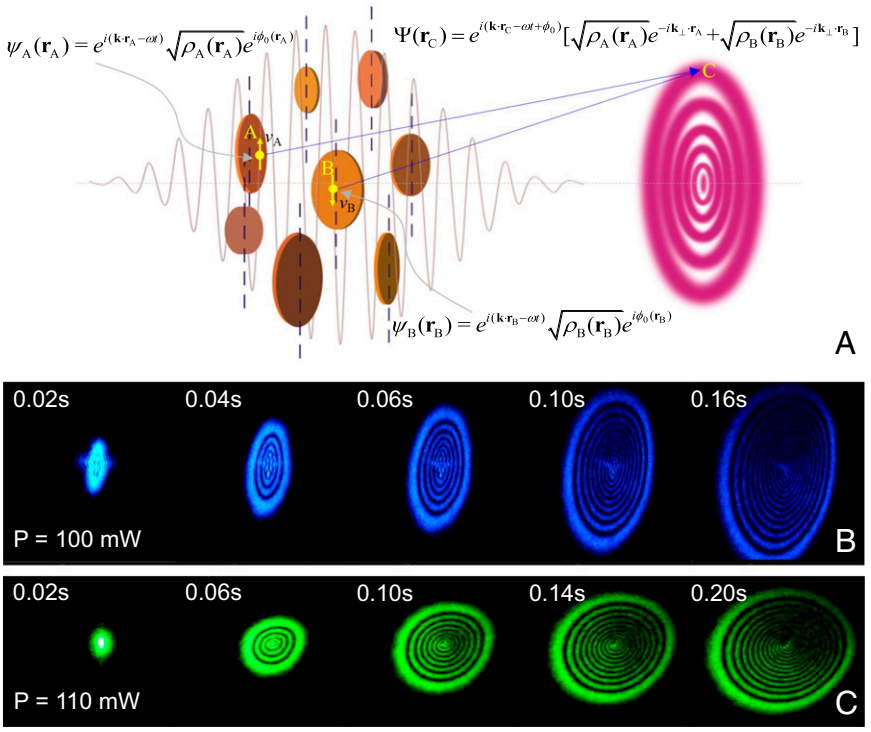

Fig. 3. Wind-chime model and the emergence of electron coherence. (*A*, *Left*) Collective response of the MoS_2 flakes to the laser beam electric field, being aligned to form a "wind chime." (*A*, *Right*) SSPM pattern formed. (*B* and *C*) Snapshots of the pattern formation at 473-nm and 532-nm laser beam excitations, respectively. The whole process takes ~0.20 s, which is consistent with the wind-chime model prediction (main text).

time for the ring formation is a strong experimental support to the wind-chime model.

We then discuss the emergence of the ac electron coherence. Writing the electronic wave function at $\mathbf{r}_A$ as $\psi_A(\mathbf{r}_A) = \sqrt{\rho_A(\mathbf{r}_A)}e^{i\phi(\mathbf{r}_A)}$, with $\psi_A^*(\mathbf{r}_A)\cdot\psi_A(\mathbf{r}_A) = \rho_A(\mathbf{r}_A)$ being the local electron density, the phase $\phi(\mathbf{r}_A) = \mathbf{k}\cdot\mathbf{r}_A - \omega t + \phi_0(\mathbf{r}_A)$ of the electronic wave function is completely determined by the external light field (Fig. 3*A*). The wave function oscillates at a frequency of $\sim 10^{14}$ Hz (i.e., optical frequency). Classically, this is a forced oscillation, where electrons have to assume the enforced local phase by the external field, even surviving scatterings and collisions. Here $\phi_0(\mathbf{r}_A)$ represents the phase lag in response to the external field. It is not the initial random phase, which is wiped off by dissipation. The same applies to the electronic wave functions at $\mathbf{r}_B$ in a different (or the same) flake. Because the two wave functions are both coherent with the light wave, they are coherent to each other too. This is a dynamic or ac electron coherence, which is different from the commonly known steady-state or dc electron coherence in transport measurements. The electrons do not move far away from their equilibrium positions. After the wind-chime formation the electron coherence becomes stronger because more electrons get correlated and fewer collisions get involved, owing to the aligned geometry. At the far field, the intensity is $I(\mathbf{r}_C) = E^*(\mathbf{r}_C)\cdot E(\mathbf{r}_C)$, where $E(\mathbf{r}_C)$ is the electric field of the light wave at $\mathbf{r}_C$. It becomes $E(\mathbf{r}_C) = \varsigma(\chi^{(3)})\Psi(\mathbf{r}_C)$, with $\Psi(\mathbf{r}_C) = e^{i(\mathbf{k}\cdot\mathbf{r}_C-\omega t+\phi_0)}[\sqrt{\rho_A(\mathbf{r}_A)}e^{-i\mathbf{k}_\perp\cdot\mathbf{r}_A} + \sqrt{\rho_B(\mathbf{r}_B)}e^{-i\mathbf{k}_\perp\cdot\mathbf{r}_B}]$ being the optical phase except for a normalization factor. Here $k_\perp = d\Delta\phi/dr$ is the wavevector generated due to the nonlinear response term of n_2 (*Methods*). The exact coefficient $\varsigma(\chi^{(3)})$ is determined by the optical nonlinearity $\chi^{(3)}$, which is comprehensively determined by the carrier properties in the material.

We found that SSPM can be used to measure easily the $\chi^{(3)}_{\text{onelayer}}$ value for many of the layered quantum materials (we have also observed SSPM in dispersion of $MoSe_2$ flakes and obtained the $\chi^{(3)}$ value). In other coherent methods (e.g., THG or FWM), the signal is much weaker than the input beam (25). Instead, in SSPM the diffracted beam is strong, owing to the intrinsic electron coherence. Significantly, SSPM can be used to measure $\chi^{(3)}$ from near IR to UV, compared with THG working only for the region where the 3 ω signal can be easily detected. This is essential for materials with a relatively large gap. In this sense we have found a powerful and ubiquitous (in some cases unique) way to measure $\chi^{(3)}$ for many of the 2D gapped quantum materials.

To quantitatively investigate the gap-dependent property, we obtained $\chi^{(3)}$ values for excitations at multiple wavelengths (Fig. 4*A*). For example $\chi^{(3)}_{\text{onelayer}}$ at 532 nm is 1.6×10^{-9} electrostatic units (e.s.u.) (i.e., 2.23×10^{-17} m^2/V^2; *Methods*), which is orders of magnitude larger than that of conventional semiconductors, owing to the high carrier density and mobility in 2D layered materials. In parallel we calculated the absorption as a function of wavelength for few-layer MoS_2, where the dipole transition is proportional to the occupation probabilities of valence and conduction bands. As shown in Fig. 4*A*, the experimental results and theoretical calculations compare well. A sharp change in $\chi^{(3)}$ and threshold values can be seen at 1.72 eV (722 nm), which is exactly the gap value of MoS_2. This gap-dependent property is a manifestation of the electronic band structure of MoS_2. Thus, SSPM can be used to investigate band structures of layered quantum materials and can be conveniently compared with other experimental methods such as absorption and photoluminescence. The SSPM method applies especially to those materials where large single crystals are not available and absorption is hard to measure.

In Fig. 4*A* the experimental results compare well with the calculated absorption along x and y, but not that along the z direction (*SI Text, section S2*). This is strong evidence that, in our experiment, light propagation is perpendicular to the x or y but not the z axis, which confirms the validity of the wind-chime model. Note that this is an even stronger restriction than the wind-chime model.

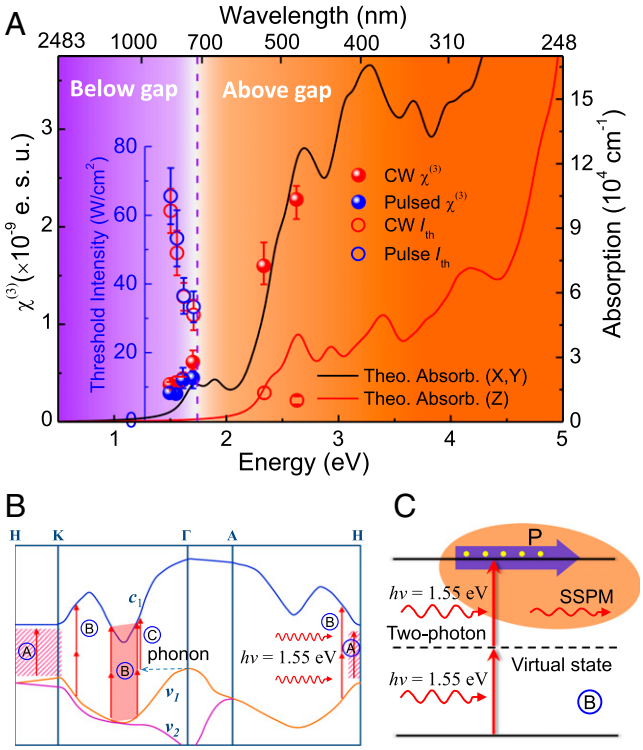

Fig. 4. Bandgap-dependent $\chi^{(3)}$ and I_{th} and the SSPM mechanisms. (*A*) Bandgap dependence of $\chi^{(3)}$ (solid spheres) and I_{th} (open circles) for ultrafast (blue) and cw (red) excitations, respectively. The calculated photoabsorption spectrum of MoS_2 is also shown (black and red curves) for comparison. The below-gap (purple) and above-gap (orange) regions are marked. (*B*) Scenarios of the SSPM formation mechanisms: Ⓐ Single-photon absorption-induced SSPM; Ⓑ two-photon absorption-induced SSPM; Ⓒ indirect-bandgap phonon-assisted SSPM. The bandgap structure is adopted from ref. 2. (*C*) Two-photon absorption leads to SSPM of the fundamental beam.

Considering the plasmonic interaction due to free carriers (26), it is indeed possible that the collective behavior leads to a "frozen" wind chime, where all domains become parallel to each other and perpendicular to the direction of laser propagation. The gap-dependent nature displayed in Fig. 4 shows again that SSPM is mainly due to the various charge carriers.

The below-gap SSPM has never been reported before. Three mechanisms might be responsible for it (Fig. 4 *B* and *C*): Ⓐ single-photon SSPM with Fermi distribution smearing, Ⓑ two-photon SSPM, and Ⓒ phonon-assisted indirect-gap SSPM. For Ⓐ, it can be seen that Fermi smearing relevant for significant photoabsorption occurs only at zones near the H and K points in momentum space. For Ⓑ, the carriers generated through two-photon absorption build up an electrical polarization, which diffracts not only those photons above the gap, but also those below the gap (Fig. 4*B*). As such, even though it is a two-photon nonlinear process, one expects a linear power dependence relation because the change in refractive index is proportional to the light intensity *I*. Heuristically, the excited carriers diffract both excitation photons (i.e., two output photons). In comparison there is only one output photon in second harmonic generation and two-photon photoluminescence. Two-photon SSPM is the most likely mechanism responsible for below-gap SSPM. For Ⓒ, the indirect gap photon excitation requires assistant phonon injection (Fig. 4*C*), which usually has a very small probability. In-gap defect states are relatively sparse (resonant in-gap states are more sparse) and localized (whereby charge carriers cannot move freely and scattering occurs frequently, which ruins the acquired uniform phase), so they are unlikely a major reason for SSPM.

We further demonstrate that, in forming SSPM, free carriers generated by photons at one wavelength can diffract photons at another wavelength, as if they were generated by the latter photons. The experimental setup is illustrated in Fig. 5*C*, which demonstrates a two-color (473 nm and 532 nm) SSPM. When we fix the power of one beam (even below threshold) and increase that of the other, the ring number and diameter for each beam both increase simultaneously. The brightness decreases, with the total intensity remaining unchanged, and energy conservation is preserved (Fig. 5*D*). In Fig. 5*B* the ring number of the 473-nm pattern exhibits linear dependence on the sum of the two beam powers, although the intensity of the 473-nm beam is fixed. The same is true for the 532-nm ring (*SI Text, section S3*). Once the coherence is correlated, each beam experiences the SSPM—as if the free carriers are created by the beam itself. Fig. 5*A* is an overall illustration of this property. This indistinguishability helps explain why in two-photon SSPM one can still have linear dependence and still obtain a relatively large $\chi^{(3)}$.

Significantly, our experiment is to our knowledge the first demonstration of all-optical switching based on SSPM. Because the switching beam is controlling the phase of the other one, a small change in intensity will result in the shift of the strong signal pattern in real space, where a detector is placed. The detector can be made to detect the whole rings. Thus, a weaker beam can switch on and off a stronger beam (27, 28). Quantitatively taking the intensity of the signal beam (strong beam) at 473 nm to be $I_{strong} = 120$ W/cm^2, the intensity of the control beam (weak beam) at 532 nm needs only to be $I_{weak} = 2.0$ W/cm^2 to change the phase of the strong beam by π (i.e., $\Delta N = 0.5$, Fig. 2). Hence to make an all-optical switch with full contrast ratio, I_{weak}:I_{strong} = 1:60. This is characteristic of weak-control–strong all-optical switching, which is apparently cascade possible (27, 28).

It is interesting that in the experiment intraband electron coherence has been correlated between photocarriers of 473-nm and 532-nm excitations. We note that similar coherence is also induced among the holes, the excitons, and the free electron–hole pairs. The two-color switching can further enable high-contrast-ratio operations, because in two-color operation optical filters can be used to block the signal beam. Two-color switching also makes it possible for multichannel mixed switching and thus enables very broad-band optoelectronic devices. We leave additional details of the SSPM-based all-optical switching to future investigations. In summary, our experiment demonstrates an all-optical switching based on SSPM, with the advantages including a weak-control–strong, cascade-possible, high-contrast-ratio, room-temperature device; broadband functioning; condensed state; and particularly broad-band-accessible quantum materials.

Conclusions

In conclusion, nonlocal ac electron coherence among different flake domains of MoS_2 has been optically correlated based on SSPM. A wind-chime model is proposed to account for this emergent collective behavior, which is verified by experimental observation of the pattern formation time. Significantly, gap-dependent SSPM has been observed, where the $\chi^{(3)}$ value and the threshold I_{th} both show abrupt changes across the MoS_2 bandgap. Mechanisms including two-photon SSPM have been discussed. Furthermore, we have experimentally demonstrated all-optical switching based on SSPM, which employs the intraband electron coherence. Our investigation signifies a ubiquitous property of 2D layered quantum materials and extends their potentials in optoelectronic applications by realizing all-optical switching.

Methods

Ultrafast and cw Experiment of SSPM in MoS_2. Multiple ultrafast and cw laser beams were used to investigate the SSPM from suspended MoS_2 flakes. In the ultrafast experiment, 800-nm light pulses of 200-fs pulse width and 80-MHz repetition rate were focused onto the sample. The solvent is acetone and the container is a 1-cm-thick cuvette. The distance between the focusing lens

PHYSICS

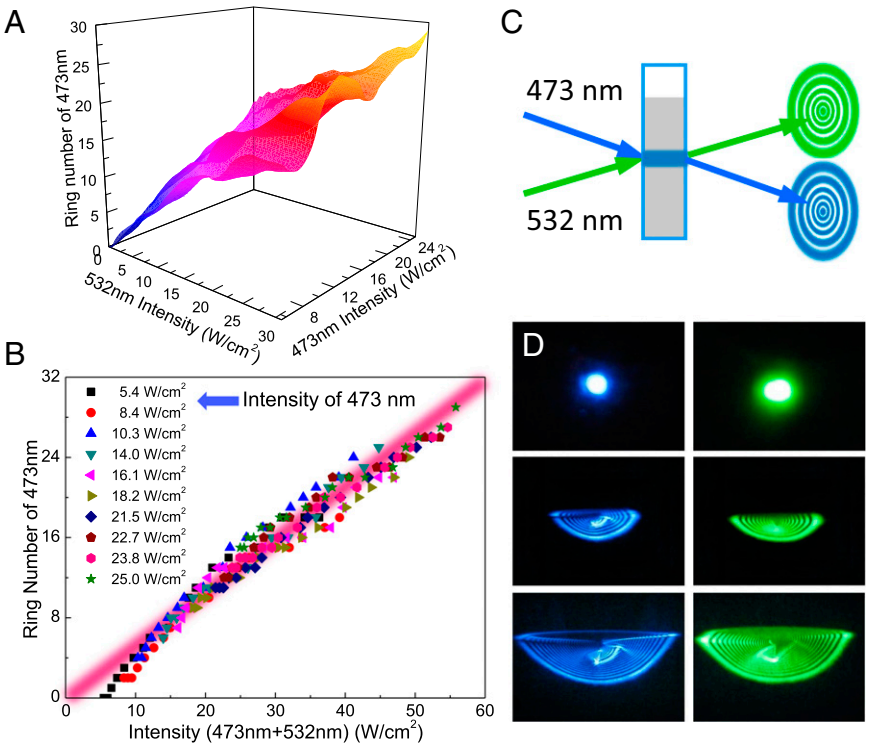

Fig. 5. All-optical switching based on SSPM. (*A* and *B*) Dependence of the 473-nm beam ring number on the sum intensity. (*C*) Schematic of the switch. (*D*) Generating the 473-nm pattern by increasing the 532-nm beam intensity. Both ring numbers (and diameters) increase simultaneously, with fixed 473-nm intensity below threshold.

($f = 200$ mm) and the center of the cuvette is kept fixed at 150 mm. The beam spot size after focusing is 0.2 mm for the $1/e^2$ intensity radius. In the cw experiment, single transverse-mode 532-nm and 473-nm laser beams were used instead, having a similar beam spot size on the sample. The relation between the fringe thickness and the flake concentration is investigated and discussed in *SI Text, section S4*. Micrometer-sized powder of MoS_2 crystals (LSKYD, www.kydmaterials.com/en/index.php) was added into the solvent and then ultrasonicated for 30 min before the measurement. The optimum concentration is 0.14 g/L (i.e., 8.5×10^{-4} mol/L). From our Raman and absorption characterization there are very few monolayer MoS_2 flakes in our sample (*SI Text, section S5*). From Fig. 1*B*, it can be seen that our sample is mainly composed of MoS_2 flakes with a thickness of $30 \sim 55$ layers. Being different from the linear optical phenomena of Newton's rings, the SSPM pattern has a finite number of fringes and the thickest fringe has the largest diameter. The critical proof of observing a SSPM pattern is that the number of rings, N, increases linearly with the input laser intensity.

Fundamentals of SSPM and the Calculation of the $\chi^{(3)}_{\text{onelayer}}$ in MoS_2. The nonlinear optical response SSPM is characterized by $n = n_0 + n_2 I$, where n_0 and n_2 are the linear and nonlinear refractive indexes, respectively. Assuming a Gaussian beam, the optical phase accumulated after propagation length l is $\Delta\psi(r) = (2\pi n_0/\lambda)\int_{-l/2}^{l/2} n_2 I(r,z)dz$, where z is the propagation direction of the incident laser beam. Thus, we have $\Delta\psi(0) - \Delta\psi(\infty) = (2\pi n_0/\lambda)n_2 \cdot 2I \cdot l$, with $I(0, z) = 2I$. The number of rings N is proportional to the phase change in the output beam ($\Delta\psi(0) - \Delta\psi(\infty) = 2\pi N$), leading to $n_2 = (\lambda/2n_0 l)(N/I)$, where $n_0 = 1.36$ and N is proportional to I for a nearly constant n_2. By the slope in Fig. 2 we can straightforwardly obtain n_2 from the experimental data. With $n_2 = (12\pi^2/(n_0^2 c))10^3\chi^{(3)}$ (in the SI unit) we estimate that $\chi^{(3)} = 1.44 \times 10^{-4}$ e.s.u. for the 532-nm cw laser beam excitation. The number of effective single layers, M, that the laser beam passes through is estimated to be about 300, using the concentration of the sample (*SI Text, section S6*). As $I_{\text{total}} \sim M^2 I_{\text{onelayer}}$, we estimate that $\chi^{(3)} = M^2\chi^{(3)}_{\text{onelayer}}$. The estimated $\chi^{(3)}_{\text{onelayer}}$ for 532 nm is 1.6×10^{-9} e.s.u. (i.e., 2.23×10^{-17} m^2/V^2).

Conveyance of the ac Electron Coherence to the Optical Coherence. The diffraction of the beam off the z axis is due to a finite perpendicular wavevector, which is, for a Gaussian beam $\Delta\psi(r) = \Delta\psi(0)\exp(-2r^2/a^2)$, explicitly written as $k_\perp = d\Delta\psi(r)/dr = (-16\pi n_0 n_2 Il/a^2\lambda)r \cdot \exp(-2r^2/a^2)$. After the wind chime is formed, the optical coherence forming the fringes is conveyed from the electron coherence:

$$\begin{aligned}\Psi(\mathbf{r}_C) &= \left[\sqrt{\rho_A(\mathbf{r}_A)}e^{i\phi(\mathbf{r}_A)}e^{i|\mathbf{k}_z\cdot(\mathbf{r}_C-\mathbf{r}_A)|}e^{i\left[\nabla_{r_\perp}(\Delta\phi)|_{\mathbf{r}_A}\right]\widehat{r_\perp}\cdot(\mathbf{r}_C-\mathbf{r}_A)}\right.\\ &\quad\left.+\sqrt{\rho_B(\mathbf{r}_B)}e^{i\phi(\mathbf{r}_B)}e^{i|\mathbf{k}_z\cdot(\mathbf{r}_C-\mathbf{r}_B)|}e^{i\left[\nabla_{r_\perp}(\Delta\phi)|_{\mathbf{r}_B}\right]\widehat{r_\perp}\cdot(\mathbf{r}_C-\mathbf{r}_B)}+\ldots\right]\\ &= e^{i(\mathbf{k}_z\cdot\mathbf{r}_C-\omega t)}\left[\sqrt{\rho_A(\mathbf{r}_A)}e^{i\phi_0(\mathbf{r}_A)}e^{i\left[\nabla_{r_\perp}(\Delta\phi)|_{\mathbf{r}_A}\right]\widehat{r_\perp}\cdot(\mathbf{r}_C-\mathbf{r}_A)}\right.\\ &\quad\left.+\sqrt{\rho_B(\mathbf{r}_B)}e^{i\phi_0(\mathbf{r}_B)}e^{i\left[\nabla_{r_\perp}(\Delta\phi)|_{\mathbf{r}_B}\right]\widehat{r_\perp}\cdot(\mathbf{r}_C-\mathbf{r}_B)}+\ldots\right]\\ &= e^{i(\mathbf{k}\cdot\mathbf{r}_C-\omega t+\phi_0)}\left[\sqrt{\rho_A(\mathbf{r}_A)}e^{-i\,\mathbf{k}_\perp\cdot\mathbf{r}_A}+\sqrt{\rho_B(\mathbf{r}_B)}e^{-i\,\mathbf{k}_\perp\cdot\mathbf{r}_B}+\ldots\right].\end{aligned}$$

Here we have taken that ϕ_0 is identical for $\mathbf{r}_A$ and $\mathbf{r}_B$, and only identical $\boldsymbol{k}_\perp$ can produce interference rings.

ACKNOWLEDGMENTS. We acknowledge useful discussion with C.-K. Shih, James Hinton, and Joseph Orenstein. This work was supported by the National Basic Research Program of China (2012CB821402 and 2012CB921403), the National Natural Science Foundation of China (11274372 and 11222431), and the External Cooperation Program of the Chinese Academy of Sciences (GJHZ1403).

1. Novoselov KS, et al. (2004) Electric field effect in atomically thin carbon films. *Science* 306(5696):666–669.
2. Mak KF, Lee C, Hone J, Shan J, Heinz TF (2010) Atomically thin MoS_2: A new direct-gap semiconductor. *Phys Rev Lett* 105(13):136805.
3. Xu XD, Yao W, Xiao D, Heinz TF (2014) Spin and pseudospins in layered transition metal dichalcogenides. *Nat Phys* 10(5):343–350.
4. Kim JH, et al. (2014) Ultrafast generation of pseudo-magnetic field for valley excitons in WSe_2 monolayers. *Science* 346(6214):1205–1208.
5. Xiao D, Liu GB, Feng W, Xu X, Yao W (2012) Coupled spin and valley physics in monolayers of MoS_2 and other group-VI dichalcogenides. *Phys Rev Lett* 108(19):196802.
6. Mak KF, et al. (2013) Tightly bound trions in monolayer MoS_2. *Nat Mater* 12(3):207–211.
7. Jones AM, et al. (2014) Spin–layer locking effects in optical orientation of exciton spin in bilayer WSe_2. *Nat Phys* 10(2):130–134.
8. Zeng H, Dai J, Yao W, Xiao D, Cui X (2012) Valley polarization in MoS_2 monolayers by optical pumping. *Nat Nanotechnol* 7(8):490–493.

9. Xiao D, Yao W, Niu Q (2007) Valley-contrasting physics in graphene: Magnetic moment and topological transport. *Phys Rev Lett* 99(23):236809.
10. Basov DN, Fogler MM, Lanzara A, Wang F, Zhang YB (2014) Colloquium: Graphene spectroscopy. *Rev Mod Phys* 86(3):959–994.
11. Novoselov KS, et al. (2005) Two-dimensional atomic crystals. *Proc Natl Acad Sci USA* 102(30):10451–10453.
12. Coleman JN, et al. (2011) Two-dimensional nanosheets produced by liquid exfoliation of layered materials. *Science* 331(6017):568–571.
13. Fei Z, et al. (2012) Gate-tuning of graphene plasmons revealed by infrared nano-imaging. *Nature* 487(7405):82–85.
14. Wu R, et al. (2011) Purely coherent nonlinear optical response in solution dispersions of graphene sheets. *Nano Lett* 11(12):5159–5164.
15. Hendry E, Hale PJ, Moger J, Savchenko AK, Mikhailov SA (2010) Coherent nonlinear optical response of graphene. *Phys Rev Lett* 105(9):097401.
16. Singh A, et al. (2014) Coherent electronic coupling in atomically thin $MoSe_2$. *Phys Rev Lett* 112(21):216804.
17. Kumar N, et al. (2013) Third harmonic generation in graphene and few-layer graphite films. *Phys Rev B* 87(12):121406.
18. Ge S, et al. (2014) Coherent longitudinal acoustic phonon approaching THz frequency in multilayer molybdenum disulphide. *Sci Rep* 4:5722.
19. Cheng JL, Vermeulen N, Sipe JE (2014) Third order optical nonlinearity of graphene. *New J Phys* 16:053014.
20. Mankowsky R, et al. (2014) Nonlinear lattice dynamics as a basis for enhanced superconductivity in $YBa_2Cu_3O_{6.5}$. *Nature* 516(7529):71–73.
21. Berg E, et al. (2007) Dynamical layer decoupling in a stripe-ordered high-T_c superconductor. *Phys Rev Lett* 99(12):127003.
22. Durbin SD, Arakelian SM, Shen YR (1981) Laser-induced diffraction rings from a nematic-liquid-crystal film. *Opt Lett* 6(9):411–413.
23. Kappera R, et al. (2014) Phase-engineered low-resistance contacts for ultrathin MoS_2 transistors. *Nat Mater* 13(12):1128–1134.
24. Sie EJ, et al. (2014) Valley-selective optical Stark effect in monolayer WS_2. *Nat Mater* 14(3):290–294.
25. Wang R, et al. (2014) Third-harmonic generation in ultrathin films of MoS_2. *ACS Appl Mater Interfaces* 6(1):314–318.
26. Bian F, et al. (2010) Laser-driven silver nanowire formation: Effect of femtosecond laser pulse polarization. *Chin Phys Lett* 27(8):088101.
27. Han XF, et al. (2008) Single-photon level ultrafast all-optical switching. *Appl Phys Lett* 92(15):151109.
28. Dawes AMC, Illing L, Clark SM, Gauthier DJ (2005) All-optical switching in rubidium vapor. *Science* 308(5722):672–674.
29. Shi H, et al. (2013) Exciton dynamics in suspended monolayer and few-layer MoS_2 2D crystals. *ACS Nano* 7(2):1072–1080.
30. Lee C, et al. (2010) Anomalous lattice vibrations of single- and few-layer MoS_2. *ACS Nano* 4(5):2695–2700.

Supporting Information

Wu et al. 10.1073/pnas.1504920112

SI Text

S1) Derivation of the Wind-Chime Model

Each pulse generates an angular momentum on each MoS_2 flake that makes them rotate unless they develop an axis parallel to the laser beam polarization. This is also associated with rotation of a small portion of the liquid nearby the flake surface. Then, the viscous force at the flake edge reduces the angular velocity exponentially until it becomes static. When the next pulse arrives, the same process repeats, where the integrated result is the macroscopic angular motion of the flake (i.e., the formation of the wind chime).

Taking $E(z,t)=E_0e^{-((ct-z)^2/c^2\tau^2)}\sin(kz-\omega_0 t)$, where τ is pulse width, we have $I=\overline{\varepsilon E^2}c=(c/2T)\varepsilon_0E_0^2\tau\sqrt{\pi/2}$, where T is the period of pulse repetition and we have assumed $2\pi/\omega_0 << \tau$. The electrical polarization in the flake domain is $\boldsymbol{P}=(\varepsilon_r-1)\varepsilon_0\boldsymbol{E}\cos\theta$. In molybdenum disulfide the electrical field is $\boldsymbol{E}/\varepsilon_r$. Thus, assuming a circular disk shape for the flake domains, the rotation torque generated by the laser pulse $\mathcal{M}=\int|\boldsymbol{P}\times\boldsymbol{E}|\,dV$ has a magnitude of

$$\mathcal{M}=\frac{1}{4}\sin 2\theta\frac{(\varepsilon_r-1)}{\varepsilon_r}\varepsilon_0E_0^2\pi R^2he^{-\left(2(ct-z)^2/c^2\tau^2\right)}, \qquad [S1]$$

where R is the disk radius and h is the disk thickness. Thus, when a pulse traverses the disk, the initial angular velocity acquired is

$$\Omega_0=\frac{\int\mathcal{M}dt}{J_{MoS_2}+J_{Solution}}=\frac{\frac{1}{4}\sin 2\theta\frac{(\varepsilon_r-1)}{\varepsilon_r}\varepsilon_0E_0^2\pi R^2h\sqrt{(\pi/2)}\tau}{J_{MoS_2}+J_{Solution}}. \qquad [S2]$$

Considering Newton's fluid with constant viscosity coefficient η and linear velocity v at the interface between the rotating and nonrotating parts, the rotation torque $\mathcal{V}$ due to the viscous force is

$$\mathcal{V}=\eta\int_0^\pi\frac{dv}{dr}(R\sin\varphi)(\xi\cdot 2\pi R\sin\varphi)(Rd\varphi)=\pi\eta\Omega\xi R^3, \qquad [S3]$$

where Ω is the rotation velocity and ξ is the portion of the globe that is rotating together with the disk. Here ξ assumes a value between 0 and 1 and we estimate it to be closer to 0, because for each pulse the rotation has to be slow and not much fluid will sense the rotation before it reaches the static state. Hence in the relaxation process induced by the viscous force we obtain $\Omega=\Omega_0e^{-(\pi\eta\xi R^3/(J_{MoS_2}+J_{Solution}))t}$. With Eq. **S2**, the rotation angle accumulated due to each single light pulse is thus

$$\delta\theta=\int_0^T\Omega dt\approx\int_0^\infty\Omega_0e^{-\left(\pi\eta\xi R^3/\left(J_{MoS_2}+J_{Solution}\right)\right)t}dt=\frac{(\varepsilon_r-1)}{\varepsilon_r}\frac{2TIh}{4\eta\xi Rc}\sin 2\theta. \qquad [S4]$$

The time for the pattern formation is

$$\sum_{i=1}^N\delta\theta_i=\frac{(\varepsilon_r-1)}{\varepsilon_r}\frac{2TIh}{4\eta\xi Rc}\cdot N\cdot\overline{\sin 2\theta_i}, \qquad [S5]$$

where N is the number of laser pulses. Assume that the pattern formation time is approximately that needed for a flake at $3\pi/8$ to rotate to $\pi/8$. Thus, we have $\overline{\sin 2\theta_i}\sim 0.86$ and $\sum_{i=1}^N\Delta\theta_i=\pi/4$. Therefore, the time needed for the pattern formation is

$$\mathcal{T}=N\cdot T=\frac{\varepsilon_r\pi\eta\xi Rc}{1.72(\varepsilon_r-1)Ih}=0.3\text{ s}, \qquad [S6]$$

where we have used the values $\varepsilon_r=3.33$ for MoS_2, $\eta=3.2\times10^{-4}$ Pa·s for acetone, $R\sim 1$ μm, $h\sim 10$ nm, $I=250$ W/cm^2, and $\xi\sim 0.03$ in our experiment. As a result, $\mathcal{T}$ does not depend on the laser repetition rate. In the extreme condition when the rate is approaching infinity, the above derivation approximately accounts for the case of a continuous wave laser beam excitation. So we have actually considered situations of both pulsed and cw laser beam excitations and the results are identical. This has been verified in our experiment. Note that apparently T is inversely proportional to the laser intensity. However, the value of ξ is somehow positively correlated to the intensity at a certain range of I. So the actual time T is not tightly dependent on the laser intensity either, which has also been confirmed in our experiment.

S2) Comparison of $\chi^{(3)}$ with Calculated Absorption Along z

From Fig. S1 it can be seen that our experimental results do not compare well with the theoretical absorption along z. At below 2 eV, the measured values are a few times higher than that of the theoretical calculation.

S3) Ring Number of the 532-nm Pattern as a Function of the Total Laser Intensity

In the main text we discussed the ring number of the 473-nm pattern. Here we show the other aspect of the same data (Fig. 5*A*) by illustrating the ring number of the 532-nm pattern (Fig. S2).

S4) Relation Between the Fringe Thickness and the Flake Concentration

As shown in Fig. S3*A* (*Upper* panel is adopted from ref. 22 and *Lower* panel is adopted from ref. 14), the fringes are interfering results of the output beams having an identical wavevector. The width of the ring peak is determined by, for a given angle change in the wavevector, how much phase change is occurring ($k_\perp(r)=d\Delta\psi(r)/dr$). The larger $\chi^{(3)}$ is (or equivalently n_2), the more phase change, and hence the narrower the fringe. It is worth noting that both the bright and dark fringes change simultaneously. If more MoS_2 flakes are under illumination, the width becomes narrower due to enhanced $\chi^{(3)}=\chi^{(3)}_{total}$.

In Fig. S3*B* we show the results from two different samples. Fig. S3*B*, *Left* corresponds to a sample that has 85% MoS_2 concentration of that of Fig. S3*B*, *Right*; thus there are 85% MoS_2 flakes illuminated. All other factors of the experiment, including the screen and camera positions, are identical. Thus, $\chi^{(3)}_{left}=(M_{left}/M_{right})^2\chi^{(3)}_{right}$, number of rings $N_{left}=(M_{left}/M_{right})^2N_{right}$, and ring diameter $D_{left}=(M_{left}/M_{right})^2D_{right}$, where M is the effective number of MoS_2 layers [note that in *Methods* we have $\chi^{(3)}=M^2\chi^{(3)}_{onelayer}$]. In Fig. S3*B*, the ring diameter is enlarged by $(M_{right}/M_{left})^2=(1/0.85)^2=1.4\times$ and the number of rings is also enlarged by 1.4×. Therefore, the absolute ring thickness is unchanged (parallel white straight lines in Fig. S3*B*). However, the relative fringe thickness is narrowed: Because the number of rings is enlarged by 1.4×, the relative fringe thickness (absolute thickness divided by the ring diameter D) is narrowed by 1.4×, too. Conversely, if one takes the jth ring counted from the ring center, both its absolute and relative thicknesses are narrowed.

S5) Absorption and Raman Spectra of the MoS_2 Flakes

The absorbance of our MoS_2 suspension is shown in Fig. S4*A*. It is different from that in ref. 2. Rather, it can be understood based on the results in ref. 29. In ref. 29 red shift has been observed for the multilayer samples. The red shift in the absorption peak of our result demonstrates that most of the flakes in our sample are not monolayer MoS_2 flakes. Here the suspension modifies the background tendency of the absorption. We also measured the Raman scattering of the flakes from the suspension (Fig. S4*B*). Comparison with that in ref. 30 shows that our sample is composed mainly of few-layer MoS_2 flakes.

S6) Estimation of the Sample Concentration

The concentration of our MoS_2 suspension solution is ρ = 0.00085 mol/L. The volume is $V = 4 \times 10^{-3}$ L. Thus, the total number of molecules in our solution is $M = \rho \times V \times N_A = 2 \times 10^{18}$. The space group of bulk MoS_2 is $P6_3/mmc$ hexagonal and the lattice constants are a = 3.161 Å and c = 12.295 Å, respectively. Thus, a single effective layer contains $m = S$/unit cell area in ab section = 1×4 cm^2/(sin 60°) × (3.161)^2 Å^2 = 4.6×10^{15} molecules. Hence the layer number is n = M/m = 444. Due to the instability of the suspension, we estimate the effective layer number to be 300.

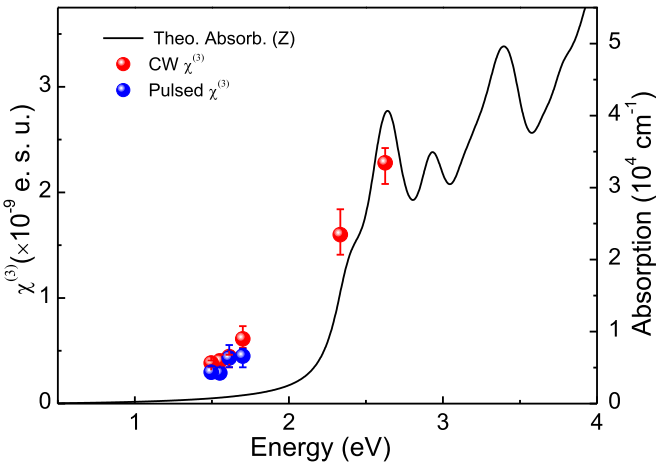

Fig. S1. Comparison of the gap-dependent $\chi^{(3)}$ with the calculated absorption. The blue and red spheres represent the pulsed and cw laser excitation results.

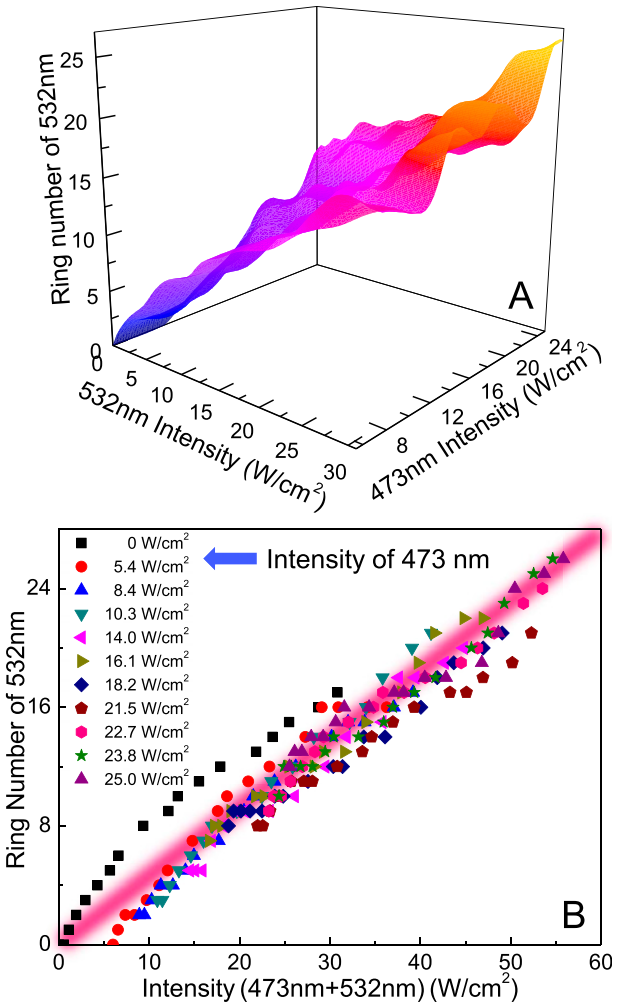

Fig. S2. Two-color all-optical switching based on SSPM. (*A* and *B*) Ring number of the 532-nm pattern, which is proportional to the sum intensity of the 532-nm and 473-nm laser beams. (*A*) Three-dimensional plotting of the results in *B*. (*B*) Data of multiple 473-nm laser fluences. The wide diagonal red line is a guide to the eye.

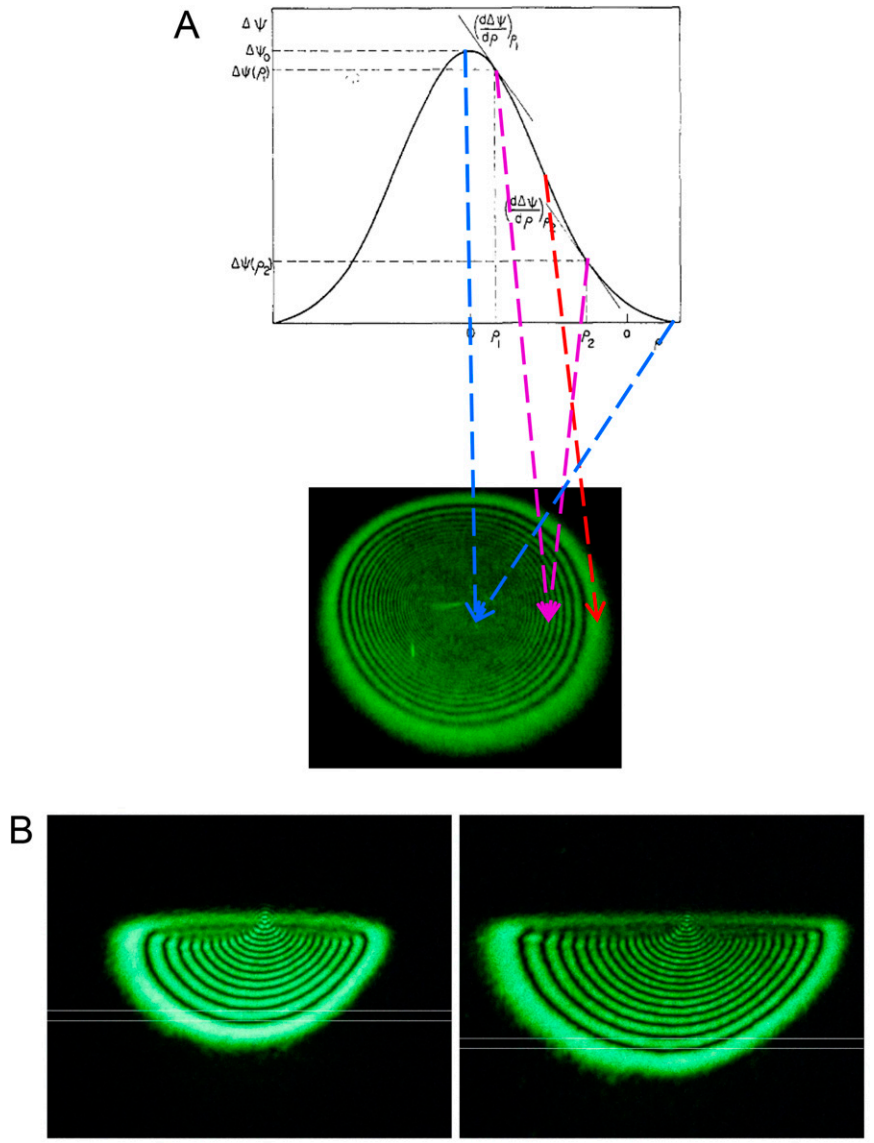

Fig. S3. Sample density dependence of the fringe thickness. (*A*) Illustration of the parallel wavevector and fringe formation. Note the difference in the fringe thickness. (*B*) The fringe thickness, depending on the solution density. *B*, *Right* corresponds to a sample with higher MoS_2 density. The white lines are used to mark the absolute fringe thickness.

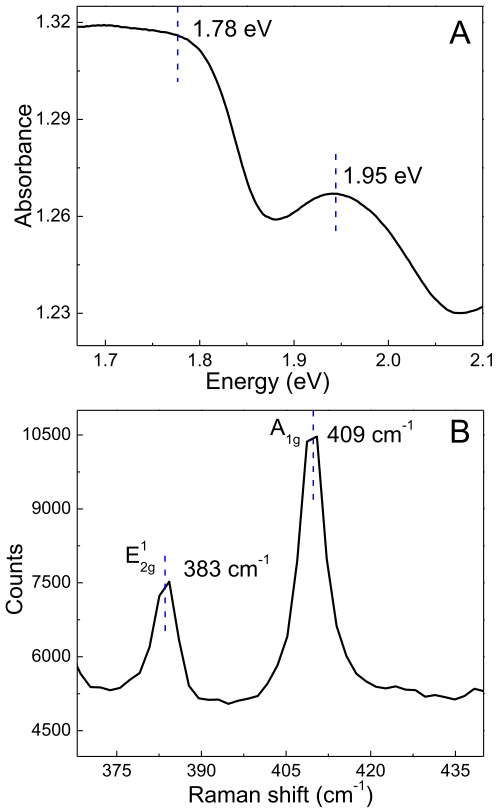

Fig. S4. Sample characterization. (*A*) Absorption spectra of the MoS_2 flake suspension. (*B*) Raman shift of the MoS_2 flakes after the evaporation of the solution.